The International Journal of Advanced Manufacturing Technology (2021) 112:1501–1512
https://doi.org/10.1007/s00170-020-06420-5

ORIGINAL ARTICLE

Milling stability prediction based on the hybrid interpolation scheme of the Newton and Lagrange polynomials

Yan Xia [1,2] · Yi Wan [1,2] · Xichun Luo [3] · Zhanqiang Liu [1,2] · Qinghua Song [1,2]

Received: 6 July 2020 / Accepted: 24 November 2020 / Published online: 3 January 2021

Abstract
The stability lobe diagram (SLD) is commonly used to determine the suitable cutting parameters of the machining system in order to achieve a chatter-free machining process. An improved full-discretization method (FDM) is proposed to predict the SLD based on the hybrid interpolation scheme of the Newton and Lagrange polynomials. In order to solve the SLD, a third-order Newton polynomial is employed to interpolate the state term of the physical space equation of the system. Meanwhile, to investigate the influence of the interpolation order on predicting the SLD, the delayed term is estimated using the Lagrange polynomials of orders one to four successively. Subsequently, after constructing the transition matrix, a series of calculation for the stability prediction are carried out by applying Floquet theory. The calculated results from these constructed methods demonstrate that the FDM with a second-order Lagrange polynomial is optimal, and further has better computational performance compared with some existing discretization methods. Lastly, the influences of the dynamic parameters on chatter stability are analyzed based on the proposed FDM. When the stiffness and damping ratio increase, the limit cutting depth will be enhanced. The increasing natural frequency not only causes an obvious shift of the lobes to the right, but also raises the limit cutting depth to some extent. These theoretical analyses can guide the prediction and improvement of the chatter stability of a machining system.

Keywords Milling stability · Delayed term · Interpolation method · Stability lobe diagram · Dynamic parameter

1 Introduction

Stability prediction is an effective way to avoid chatter in the machining process; the essence of this method is the selection of cutting parameters from the stable zone of the stability lobe diagram (SLD) [1].The SLD can be obtained by solving the delay differential equations (DDEs) used to describe the dynamic cutting process [2]. Many solution methods exist, such as the frequency domain method, numerical integration method, and discretization method [3, 4].

The zeroth-order approximation (ZOA) method presented by Altintas and Budak [5] was used to predict the milling SLD, where the force coefficients were approximated by zeroth-order Fourier series. In order to overcome the inapplicability of the ZOA method in low radial immersion conditions, they further proposed the multi-frequency method [6]. Inspired by the temporal finite element analysis method [7], Ding et al. [8] developed a numerical integration method, where the DDE was solved using the Newton-Cotes and Gauss integration formulas. Then, Liang et al. [9] proposed an improved numerical integration method, and extended it to predict the SLD when considering varying delays. Zhang et al. [10] utilized the Simpson method to calculate the SLD, and the corresponding convergence rate was improved. By using the third-order and fourth-order interpolation polynomials to replace the system state term, Ozoegwu [11] constructed the high-order vector numerical integration methods, and the results showed that the computational accuracy increased with the increase of interpolation order.

The discretization method has been widely investigated and applied as an interesting and efficient time domain method [12–30]. By equally discretizing the time period and

✉ Yi Wan
wanyi@sdu.edu.cn

[1] Key Laboratory of High Efficiency and Clean Mechanical Manufacture, Ministry of Education, School of Mechanical Engineering, Shandong University, Jinan 250061, China

[2] National Demonstration Centre for Experimental Mechanical Engineering Education, Shandong University, Jinan 250061, China

[3] Centre for Precision Manufacturing, DMEM, University of Strathclyde, Glasgow G1 1XJ, UK

approximating the delayed term with different polynomials, the zeroth-order and first-order semi-discretization methods (ZSDM and FSDM) were proposed by Insperger and Stepan, respectively [12, 13]. Then, Ding et al. [14, 15] introduced the first-order and second-order full-discretization methods (FFDM and SFDM), where the system state term was approximated by the mean of the linear interpolation and the second-order Lagrange polynomial, respectively. The calculated results showed that the convergence rate of the SFDM was better than that of the FSDM, and the FSDM converged faster than the FFDM. By using the FFDM, Zhang et al. [16] successfully predicted the chatter stability of ball-end milling. On the basis of the SFDM, Tang et al. [17] used the second-order Lagrange polynomial to interpolate the delayed term, thus improving the calculated accuracy. Further, the state, delayed, and periodic coefficient terms were approximated by the holistic-interpolation method in ref. [18]. Subsequently, third-order [19–22] and higher-order [23–25] FDMs were proposed to increase the precision of the stability prediction. In the referenced literature, the third-order Newton polynomial [19, 20] and third-order Hermite polynomial [21, 22] were used, respectively, to estimate the sate term, while the delayed term was interpolated by the Lagrange, Newton, or Hermite polynomials with different orders. Ozoegwu et al. [23, 24] proposed the least squares method to predict the SLD, where the accuracy of the method could reach to the fourth order. Zhou et al. [25] focused on the higher-order Lagrange interpolation for the delayed term. This analysis demonstrated that a method using the fourth-order Lagrange interpolation for the delayed term was effective. Dai et al. [26] presented an improved FDM based on the golden search, and the method showed higher computational efficiency compared with the traditional FDM.

In order to completely discretize all terms of the DDE including the delayed, time domain, differential, and parameter terms, Li et al. [27] presented a complete discretization scheme (CDS) by Euler's method, and the results showed that the CDS had higher efficiency when compared with SDM and FDM. The CDS was successfully applied to predict the chatter stability of turn-milling operations [28]. Xie [29] improved the accuracy and efficiency of the CDS by approximating the time periodic coefficient matrices by way of linear interpolation. Additionally, Li et al. [30] adopted the Runge-Kutta method to completely discretize the different terms of the DDE, thus improving the computational performance of the CDS.

As shown in the above references, the FDMs are usually constructed after the system state and delayed terms are expressed by the Lagrange, Newton, or Hermite polynomials [24]. The computational accuracy of the FDMs increases gradually when the interpolation order for the system state term changes from one to four [14, 15, 19, 24], and simultaneously the relative delayed term is generally replaced by the first-order Lagrange polynomial. Similarly, the influence of the order of interpolation of the delayed term on the accuracy of predicting the SLD was analyzed in ref. [25], and the system state term was expressed by a first-order Lagrange polynomial, where the proposed FDM with a fourth-order Lagrange polynomial showed the fastest convergence rate compared with those with lower orders. However, when interpolating the system state and the delayed terms by using the higher-order Hermite and Newton polynomials respectively, Ji et al. [21] proved that higher orders had no remarkable effect on computational efficiency and accuracy. The above analysis implies that there may exist an optimal combination of interpolation orders when both the system state term and the delayed term are interpolated by different high-order polynomials. In ref. [19], the Newton polynomial was used to estimate the system state term, and the delayed term was described by the first-order Lagrange polynomial. However, the higher-order interpolation for the delayed term was not investigated. Thus, the main goal of this paper is to investigate the best order combination of the Newton and Lagrange polynomials for predicting the SLD.

The remainder of this paper is organized as follows. In Section 2, the calculation methods to solve the DDE are proposed based on the mathematical model for milling dynamics, where the delayed term is approximated by the first-order, second-order, third-order, and fourth-order Lagrange interpolation polynomials, respectively. Then, the verification for the proposed FDM is performed and compared with the existing methods in Section 3. In Section 4, the influences of the dynamic parameters of the milling system on the SLD are investigated based on the proposed FDM. Finally, the conclusions from the study are revealed in Section 5.

2 Mathematical model and calculation method

Milling dynamics can be described by the DDE, with inclusion of the regenerative effect; this can be expressed by the state matrix form [14, 15].

$$\dot{\mathbf{x}}(t) = \mathbf{A}_0\mathbf{x}(t) + \mathbf{A}(t)\mathbf{x}(t) + \mathbf{B}(t)\mathbf{x}(t-T) \tag{1}$$

where $\boldsymbol{A}_0$ is the matrix that reveals the inherent characteristic of the system, $\boldsymbol{A}(t)$ and $\boldsymbol{B}(t)$ are the time-variant coefficient matrices: $\boldsymbol{A}(t) = \boldsymbol{A}(t+T)$, $\boldsymbol{B}(t) = \boldsymbol{B}(t+T)$, and T refers to the time period.

In order to solve Eq. (1), the direct integration method is employed, which is the same as in ref. [14–26]. The first step is to equally discretize the time period T into m small intervals, that is, $T = m\tau$, where the division $[k\tau, (k+1)\tau]$ represents one small time interval of T with $k = 0, 1, 2, \ldots m$. Thus, the response of Eq. (1) can be expressed by

Table 1 System parameters

Term	Notation	Value
Natural frequency	f_n	922 Hz
Damping ratio	ζ	1.1%
Modal mass	m_t	0.03993 kg
Cutting force coefficients	K_t	6×10^8 N/m^2
	K_n	2×10^8 N/m^2
Tooth number	N	2

$$\mathbf{x}(t) = e^{\mathbf{A}_0(t-k\tau)}\mathbf{x}(k\tau) + \int_{k\tau}^{t}\left\{e^{\mathbf{A}_0(t-\xi)}[\mathbf{A}(\xi)\mathbf{x}(\xi) + \mathbf{B}(\xi)\mathbf{x}(\xi-T)]\right\}d\xi \quad (2)$$

When $t = (k+1)\tau$, the x_{k+1} can be obtained as follows.

$$\mathbf{x}_{k+1} = e^{\mathbf{A}_0\tau}\mathbf{x}(k\tau) + \int_0^{k\tau}\left\{e^{\mathbf{A}_0\xi}\begin{bmatrix}\mathbf{A}(k\tau+\tau-\xi)\mathbf{x}(k\tau+\tau-\xi)+\\ \mathbf{B}(k\tau+\tau-\xi)\mathbf{x}(k\tau+\tau-\xi-T)\end{bmatrix}\right\}d\xi \quad (3)$$

Then, the system state, periodic coefficient, and delayed terms are estimated using different interpolation polynomials. In the small time interval of $k\tau \le t \le (k+1)\tau$, the periodic coefficient terms $\boldsymbol{A}(k\tau+\tau-\xi)$ and $\boldsymbol{B}(k\tau+\tau-\xi)$ are estimated by the two end values in the form of a first-order Lagrange interpolated polynomial, which can be described by

$$\begin{aligned}\mathbf{A}(k\tau+\tau-\xi) &= \dot{\mathbf{A}}_0^{(k)} + \mathbf{A}_1^{(k)}\xi \\ \mathbf{B}(k\tau+\tau-\xi) &= \dot{\mathbf{B}}_0^{(k)} + \mathbf{B}_1^{(k)}\xi\end{aligned} \quad (4)$$

with

$$\begin{aligned}\mathbf{A}_0^{(k)} &= \mathbf{A}_{k+1}\mathbf{A}_1^{(k)} = \frac{\mathbf{A}_k-\mathbf{A}_{k+1}}{\tau} \\ \mathbf{B}_0^{(k)} &= \mathbf{B}_{k+1}\mathbf{B}_1^{(k)} = \frac{\mathbf{B}_k-\mathbf{B}_{k+1}}{\tau}\end{aligned} \quad (5)$$

Here, $\boldsymbol{A}_k$ and $\boldsymbol{A}_{k+1}$ represent the values at the time points $t = k\tau$ and $(k+1)\tau$, respectively.

According to the third-order Newton polynomial, four state values $\mathbf{x}_{k+1}$, $\mathbf{x}_k$, $\mathbf{x}_{k-1}$, and $\mathbf{x}_{k-2}$ are used to interpolate the system state term in Eq. (3), which can be described by

$$\mathbf{x}(k\tau+\tau-\xi) = a_0\mathbf{x}_{k+1} + b_0\mathbf{x}_k + c_0\mathbf{x}_{k-1} + d_0\mathbf{x}_{k-2} \quad (6)$$

with

$$\begin{aligned}a_0 &= -\frac{\xi^3}{6\tau^3} + \frac{\xi^2}{\tau^2} - \frac{11\xi}{6\tau} + 1 \\ b_0 &= \frac{\xi^3}{2\tau^3} - \frac{5\xi^2}{2\tau^2} + \frac{3\xi}{\tau} \\ c_0 &= -\frac{\xi^3}{2\tau^3} + \frac{2\xi^2}{\tau^2} - \frac{3\xi}{2\tau} \\ d_0 &= \frac{\xi^3}{6\tau^3} - \frac{\xi^2}{2\tau^2} + \frac{\xi}{3\tau}\end{aligned} \quad (7)$$

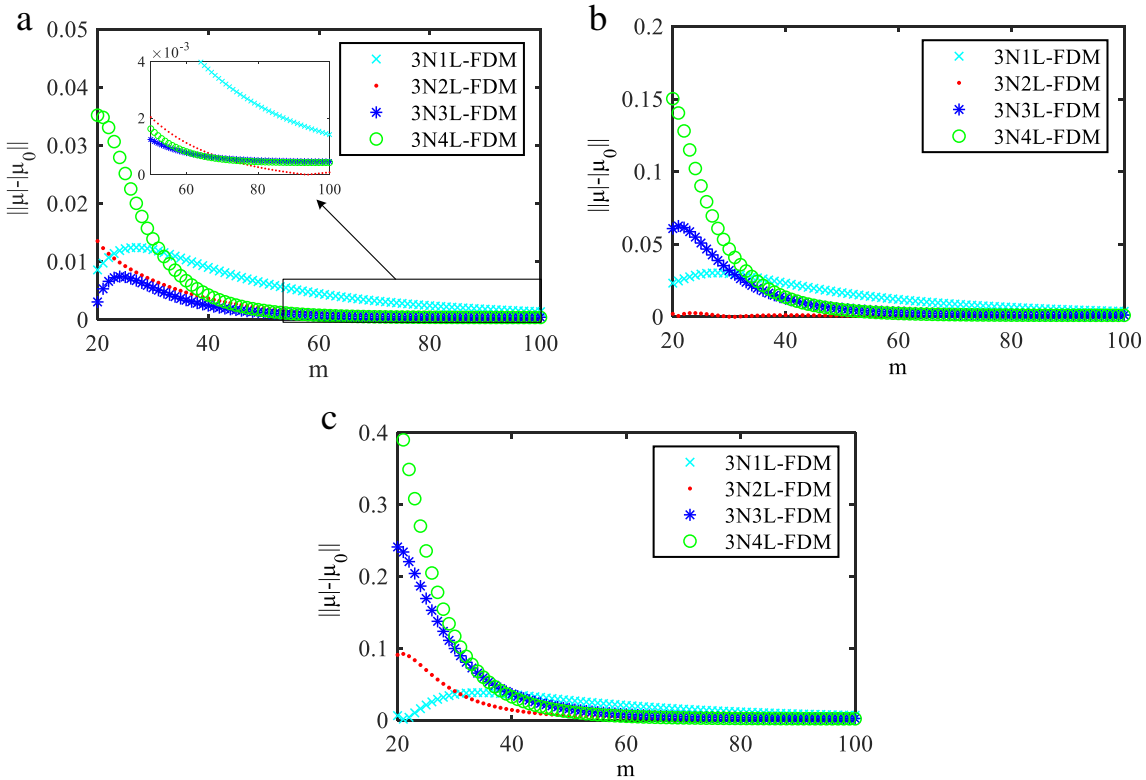

Fig. 1 Convergence rate of the eigenvalues for different approximation parameters m for the proposed FDMs when w is 0.2 mm (**a**), 0.5 mm (**b**), and 1 mm (**c**), respectively

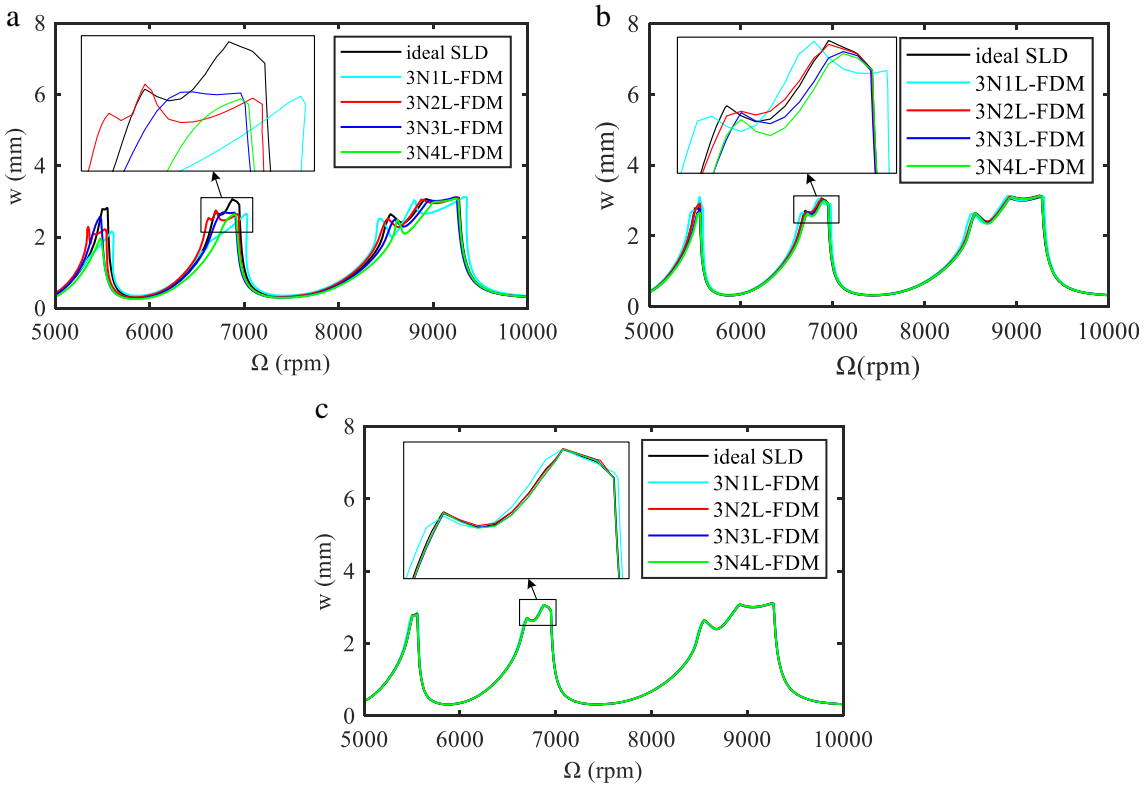

Fig. 2 The SLDs according to the proposed FDMs when m is 20 (**a**), 40 (**b**), and 80 (**c**), respectively

In order to investigate the influence of the interpolation order of the delayed term on predicting the SLD, the delayed term is approximated using the first-order, second-order, third-order, and fourth-order Lagrange polynomials, respectively, which are shown in detail in Subsections 2.1–2.4.

2.1 Case I: The Lagrange polynomial is first-order

In this case, the delayed term is approximated by a first-order Lagrange polynomial, which can be described by

$$\mathbf{x}(k\tau+\tau-\xi-T) = a_1\mathbf{x}_{\text{k-m}} + b_1\mathbf{x}_{\text{k-m+1}} \tag{8}$$

with

$$a_1 = \frac{\xi}{2} \quad b_1 = 1-\frac{\xi}{2} \tag{9}$$

Table 2 Computational time for the proposed FDMs

Methods	$m=20$	$m=40$	$m=80$
3N1L-FDM	27.7 s	80.9 s	281.1 s
3N2L-FDM	30.4 s	88.4 s	296.7 s
3N3L-FDM	33.0 s	93.2 s	311.0 s
3N4L-FDM	36.4 s	101.4 s	328.3 s

Substituting Eqs. (4), (6), and (8) into Eq. (3) generates

$$(\mathbf{I}-\mathbf{F}_{\text{k1}})\mathbf{x}_{\text{k+1}} = (\mathbf{F}_0+\mathbf{F}_{\text{k}})\mathbf{x}_{\text{k}} + \mathbf{F}_{\text{kp1}}\mathbf{x}_{\text{k-1}} + \mathbf{F}_{\text{kp2}}\mathbf{x}_{\text{k-2}} + \mathbf{F}_{\text{k1m}}\mathbf{x}_{\text{k+1-m}} + \mathbf{F}_{\text{km}}\mathbf{x}_{\text{k-m}} \tag{10}$$

When $(\boldsymbol{I}-\boldsymbol{F}_{\text{k1}})^{-1}$ exists, the discrete map can be defined as

$$\mathbf{y}_{\text{k+1}} = \mathbf{D}_{\text{k}}\mathbf{y}_{\text{k}} \tag{11}$$

Then, the transition matrix, $\boldsymbol{\Phi}$, can be expressed by a series of matrix $\boldsymbol{D}_{\text{k}}$, which can be written as

$$\mathbf{y}_{\text{m}} = \boldsymbol{\Phi}\mathbf{y}_0 \tag{12}$$

where

$$\boldsymbol{\Phi} = \mathbf{D}_{\text{m-1}}\mathbf{D}_{\text{m-2}}\cdots\mathbf{D}_1\mathbf{D}_0 \tag{13}$$

Lastly, based on Eq. (13), chatter stability can be predicted via Floquet theory [12]. Note that the symbols in Eqs. (10) and (11) are given in Appendix 1. The condition under case I is equivalent to that in ref. [19].

2.2 Case II: The Lagrange polynomial is second-order

In this case, the delayed term is interpolated by the second-order Lagrange polynomial, which can be defined as

$$\mathbf{x}(k\tau+\tau-\xi-T) = a_2\mathbf{x}_{\text{k-m}} + b_2\mathbf{x}_{\text{k-m+1}} + c_2\mathbf{x}_{\text{k-m+2}} \tag{14}$$

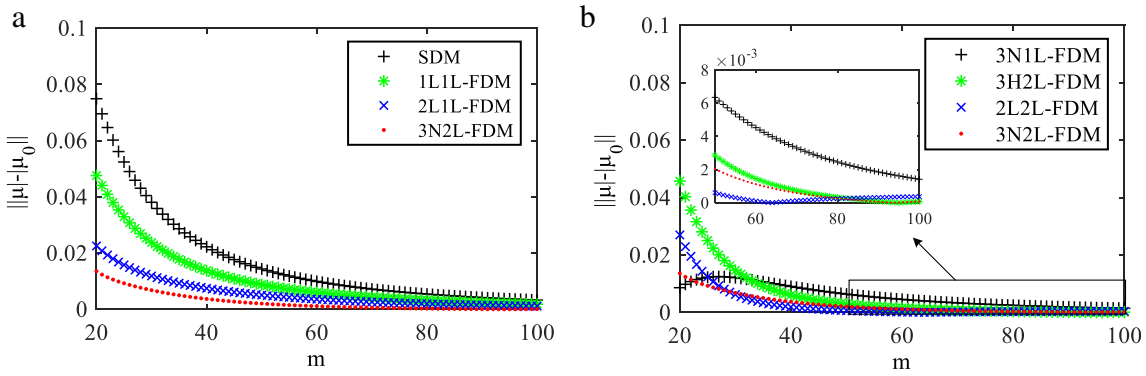

Fig. 3 Convergence rate of the eigenvalues for different approximation parameters m for the proposed 3N2L-FDM and the existing methods when w is 0.2 mm

with

$$\begin{aligned} a_2 &= \frac{\xi^2}{2\tau^2} + \frac{\xi}{2\tau} \\ b_2 &= -\frac{\xi^2}{\tau^2} + 1 \\ c_2 &= \frac{\xi^2}{2\tau^2} - \frac{\xi}{2\tau} \end{aligned} \tag{15}$$

Substituting Eqs. (4), (6), and (14) into Eq. (3) leads to

$$\begin{aligned} (\mathbf{I}-\mathbf{F}_{k1})\mathbf{x}_{k+1} = (\mathbf{F}_0 + \mathbf{F}_k)\mathbf{x}_k + \mathbf{F}_{kp1}\mathbf{x}_{k-1} + \mathbf{F}_{kp2}\mathbf{x}_{k-2} \\ + \mathbf{F}_{k2m}\mathbf{x}_{k+2-m} + \mathbf{F}_{k1m}\mathbf{x}_{k+1-m} + \mathbf{F}_{km}\mathbf{x}_{k-m} \end{aligned} \tag{16}$$

Then, according to a similar derivation process as in Subsection 2.1, the corresponding discrete matrix $\boldsymbol{D}_k$ and transition matrix, $\boldsymbol{\Phi}$, can be obtained, which are listed in Appendix 2.

2.3 Case III: The Lagrange polynomial is third-order

In case III, we use the third-order Lagrange polynomial to interpolate the delayed term, which can be represented by

$$\begin{aligned} \mathbf{x}(k\tau + \tau - \xi - T) = a_3\mathbf{x}_{k-m} + b_3\mathbf{x}_{k-m+1} + c_3\mathbf{x}_{k-m+2} \\ + d_3\mathbf{x}_{k-m+3} \end{aligned} \tag{17}$$

where

$$\begin{aligned} a_3 &= \frac{\xi^3}{6\tau^3} + \frac{\xi^2}{2\tau^2} + \frac{\xi}{3\tau} \\ b_3 &= -\frac{\xi^3}{2\tau^3} - \frac{\xi^2}{\tau^2} + \frac{\xi}{2\tau} + 1 \\ c_3 &= \frac{\xi^3}{2\tau^3} + \frac{\xi^2}{2\tau^2} - \frac{\xi}{\tau} \\ d_3 &= -\frac{\xi^3}{6\tau^3} + \frac{\xi}{6\tau} \end{aligned} \tag{18}$$

Substituting Eqs. (4), (6), and (17) into Eq. (3) yields

$$\begin{aligned} (\mathbf{I}-\mathbf{F}_{k1})\mathbf{x}_{k+1} = (\mathbf{F}_0 + \mathbf{F}_k)\mathbf{x}_k + \mathbf{F}_{kp1}\mathbf{x}_{k-1} + \mathbf{F}_{kp2}\mathbf{x}_{k-2} + \mathbf{F}_{k3m}\mathbf{x}_{k+3-m} \\ + \mathbf{F}_{k2m}\mathbf{x}_{k+2-m} + \mathbf{F}_{k1m}\mathbf{x}_{k+1-m} + \mathbf{F}_{km}\mathbf{x}_{k-m} \end{aligned} \tag{19}$$

Similarly, the discrete matrix $\boldsymbol{D}_k$ and the transition matrix, $\boldsymbol{\Phi}$, are derived, where the corresponding symbols are listed in Appendix 3.

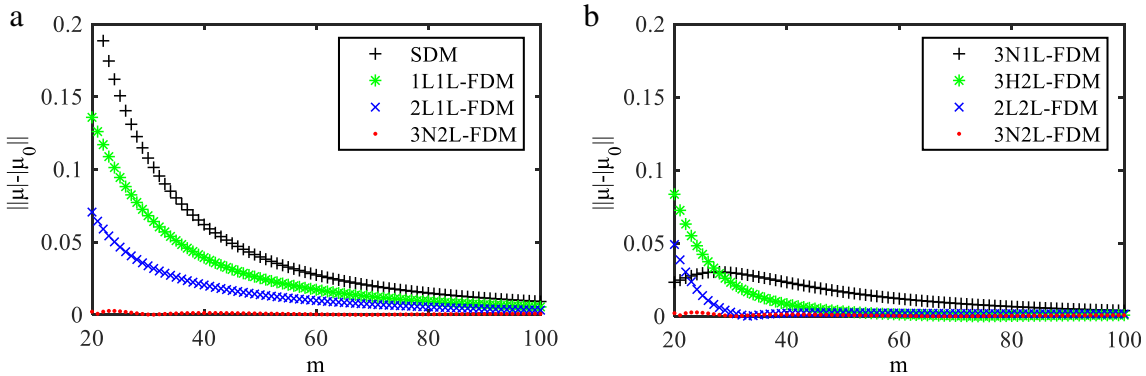

Fig. 4 Convergence rate of the eigenvalues for different approximation parameters m for the proposed 3N2L-FDM and the existing methods when w is 0.5 mm

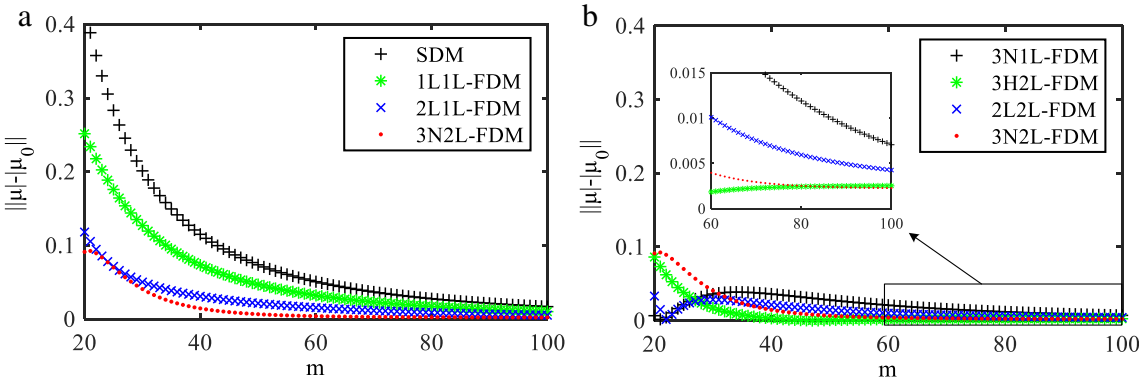

Fig. 5 Convergence rate of the eigenvalues for different approximation parameters m for the proposed 3N2L-FDM and the existing methods when w is 1 mm

2.4 Case IV: The Lagrange polynomial is fourth-order

Here, the delayed term is interpolated by the fourth-order Lagrange polynomial, which is described by

$$\mathbf{x}(k\tau+\tau-\xi-T) = a_4\mathbf{x}_{\text{k-m}} + b_4\mathbf{x}_{\text{k-m+1}} + c_4\mathbf{x}_{\text{k-m+2}} + d_4\mathbf{x}_{\text{k-m+3}} + e_4\mathbf{x}_{\text{k-m+4}} \tag{20}$$

where

$$\begin{aligned} a_4 &= \frac{\xi^4}{24\tau^4}+\frac{\xi^3}{4\tau^3}+\frac{11\xi^2}{24\tau^2}+\frac{\xi}{4\tau} \\ b_4 &= \frac{\xi^4}{6\tau^4}-\frac{5\xi^3}{6\tau^3}-\frac{5\xi^2}{6\tau^2}+\frac{5\xi}{6\tau}+1 \\ c_4 &= \frac{\xi^4}{4\tau^4}+\frac{\xi^3}{\tau^3}+\frac{\xi^2}{4\tau^2}-\frac{3\xi}{2\tau} \\ d_4 &= \frac{\xi^4}{6\tau^4}-\frac{\xi^3}{2\tau^3}+\frac{\xi^2}{6\tau^2}+\frac{\xi}{2\tau} \\ e_4 &= \frac{\xi^4}{24\tau^4}+\frac{\xi^3}{12\tau^3}-\frac{\xi^2}{24\tau^2}-\frac{3\xi}{12\tau} \end{aligned} \tag{21}$$

Substituting Eqs. (4), (6), and (20) into Eq. (3) leads to

$$(\mathbf{I}-\mathbf{F}_{\text{k1}})\mathbf{x}_{\text{k+1}} = (\mathbf{F}_0+\mathbf{F}_{\text{k}})\mathbf{x}_{\text{k}} + \mathbf{F}_{\text{kp1}}\mathbf{x}_{\text{k-1}} + \mathbf{F}_{\text{kp2}}\mathbf{x}_{\text{k-2}} + \mathbf{F}_{\text{k4m}}\mathbf{x}_{\text{k+4-m}} + \mathbf{F}_{\text{k3m}}\mathbf{x}_{\text{k+3-m}} + \mathbf{F}_{\text{k2m}}\mathbf{x}_{\text{k+2-m}} + \mathbf{F}_{\text{k1m}}\mathbf{x}_{\text{k+1-m}} + \mathbf{F}_{\text{km}}\mathbf{x}_{\text{k-m}} \tag{22}$$

Likewise, the corresponding discrete matrix $\boldsymbol{D}_{\text{k}}$ and transition matrix, $\boldsymbol{\Phi}$, are listed in Appendix 4.

3 Verification and discussion

The proposed methods are called 3N1L-FDM, 3N2L-FDM, 3N3L-FDM, and 3N4L-FDM, respectively, according to the order and name of the interpolation polynomials used to allow us to distinguish between them. Then, one benchmark example for the single degree of freedom milling model is used to verify the proposed methods. The corresponding state matrices in Eq. (1) are shown as

$$\mathbf{A}_0=\begin{bmatrix} -\zeta\omega_n & \frac{1}{m_t} \\ m_t(\zeta\omega_n)^2-m_t\omega_n^2 & -\zeta\omega_n \end{bmatrix} \quad \mathbf{A}(t)=\begin{bmatrix} 0 & 0 \\ -wh(t) & 0 \end{bmatrix} \quad \mathbf{B}(t)=\begin{bmatrix} 0 & 0 \\ wh(t) & 0 \end{bmatrix} \tag{23}$$

where these system parameters are listed in Table 1 [13–15].

In this paper, the relative calculated programs are written in MATLAB 2018a and operated on a personal computer (Intel (R) Core (TM) i5, 2.3 GHz, and 6 GB).

3.1 Comparison of the proposed FDMs

The proposed FDMs are compared to determine the optimal order of the Lagrange polynomial for the delayed term. To obtain the convergence rate, the cutting parameters from ref. [15] are selected, which include the following parameters: $\Omega = 5000$ rpm, radial immersion ratio $a/D = 1$, and a down-milling cutting depth w of 0.2 mm, 0.5 mm, and 1 mm.

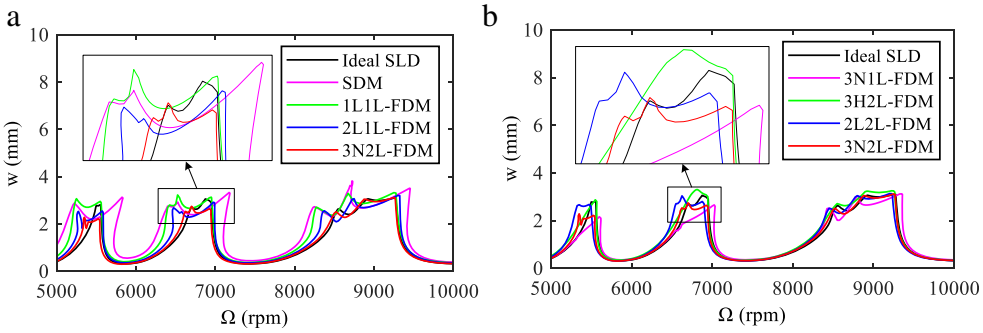

Fig. 6 The SLDs according to the proposed 3N2L-FDM and the existing methods when m is 20

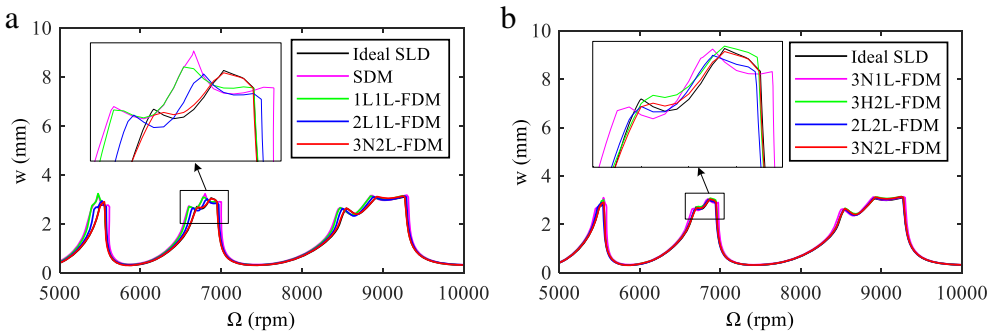

Fig. 7 The SLDs according to the proposed 3N2L-FDM and the existing methods when m is 40

Consequently, Fig. 1 shows the relationship between the eigenvalue difference $||\mu|-|\mu_0||$ and the approximation parameter m for the proposed FDMs. Here, μ_0 is the exact value of the maximal critical eigenvalues of the transition matrix when m is equal to 200. It can be observed from the figure that the convergence rates of the 3N2L-FDM are clearly faster than the others. In Fig. 1(a), the 3N3L-FDM initially converges slightly faster than the 3N2L-FDM, but the eigenvalue difference of the 3N2L-FDM is less than that of 3N3L-FDM for $m > 70$. In order to specifically demonstrate the convergence rate, m is set to 40 in Fig. 1(c), and the eigenvalue difference for the 3N2L-FDM is 0.015; to obtain the same difference, m is 72, 51, or 48 for the 3N1L-FDM, 3N3L-FDM, and 3N4L-FDM, respectively. This means that the 3N2L-FDM needs fewer time intervals, which results in its faster convergence.

The SLDs are calculated under different values of the approximation parameter m using the four FDMs in order to further determine the optimal order. The results are shown in Fig. 2. The ideal SLD (shown in black) is obtained using the method in ref. [15] for an m value of 200. In Fig. 2(a), the predicted SLDs from the four FDMs are poor approximations of the ideal SLD, since the time period is coarsely divided into only a few time intervals, whereas the red SLD from the 3N2L-FDM is comparatively a better approximation of the ideal SLD. When m increases to 40, the advantage of the accuracy of the red SLD becomes clearer, which can be seen in Fig. 2(b). As m is further increased to 80, the SLDs for the FDMs of order greater than two are nearly identical to the ideal SLD, but the SLD from the 3N1L-FDM is still obviously different from the ideal SLD.

The corresponding runtime under different m values is listed in Table 2. It can be clearly observed that the computation time for the four FDMs rapidly increases when m increases from 20 to 80. Under the same m, the efficiency of calculating SLD gradually decreases with the increase of the interpolation order for the delayed term, where the efficiency of the 3N1L-FDM is highest, and that for the 3N4L-FDM is lowest. The above analysis demonstrates that the 3N2L-FDM shows the best computational accuracy with a slight loss of computational efficiency.

This finding seems to conflict with the conclusions in ref. [25] that the precision of stability prediction could increase as the interpolation order increased. This may be because the higher-order interpolation for the system state and delayed terms gives rise to an increase of the accumulative error, which is consistent with the result in ref. [21]. Therefore, it can be understood that the higher-order polynomials used to interpolate the system state term and delayed term can increase computational time, but may not contribute to an improvement in computational accuracy.

3.2 Comparison with the existing discretization methods

To verify the effectiveness of the proposed 3N2L-FDM for predicting the SLD, a comparison between it and the existing discretization methods is essential. Several existing methods have been chosen: the zeroth-order semi-discretization method [12], first-order full-discretization method [14], second-order full-discretization method [15, 17], and third-order

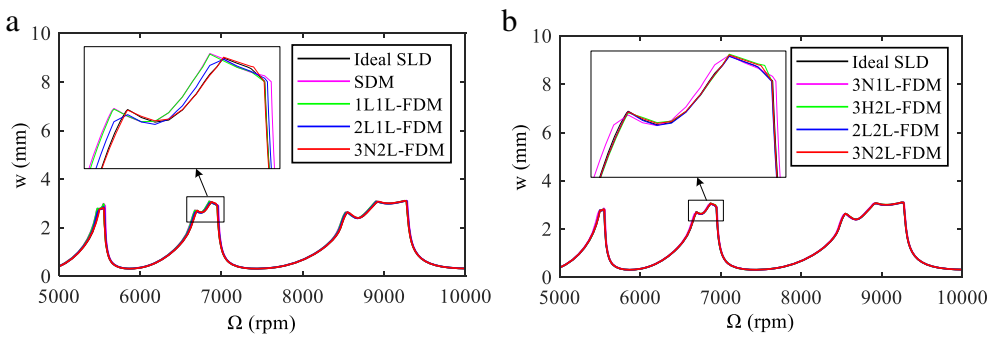

Fig. 8 The SLDs according to the proposed 3N2L-FDM and the existing methods when m is 80

Table 3 Computational time for the different discretization methods

Methods	$m = 20$	$m = 40$	$m = 80$
SDM	82.4 s	212.5 s	495.7 s
1L1L-FDM	21.9 s	66.0 s	229.8 s
2L1L-FDM	31.0 s	86.4 s	273.4 s
3N1L-FDM	37.2 s	100.8 s	300.7 s
3H2L-FDM	39.8 s	109.4 s	321.9 s
2L2L-FDM	35.4 s	96.2 s	295.3 s
3N2L-FDM	41.5 s	109.5 s	318.8 s

full-discretization method [19, 20]. In order to easily make the distinction between these methods, they are re-called as SDM [12], 1L1L-FDM [14], 2L1L-FDM [15], 2L2L-FDM [17], 3N1L-FDM [19], and 3H2L-FDM [20], respectively.

The convergence rates of these methods are first calculated and compared. The parameters used are the same as reported in Subsection 3.1. Thus, Figs. 3, 4, and 5 show the convergence rate when the cutting depth w is 0.2 mm, 0.5 mm, and 1 mm, respectively. From these figures, it can be observed that the red curves from the 3N2L-FDM converge faster than the others. However, the 2L2L-FDM in Fig. 3(b) and 3H2L-FDM in Fig. 5(b) seem to have a better convergence rate than the 3N2L-FDM. In Fig. 3(b), the convergence rate of the 2L2L-FDM initially declines, but increases when m is more than 64, and becomes larger than 3N2L-FDM when $m > 80$. Similarly, this phenomenon also occurs in Fig. 5(b). These results show that the 3N2L-FDM has better convergence stability.

The SLDs with 5000 rpm $< \Omega <$ 10,000 rpm are calculated using the previously mentioned methods, and are compared in Figs. 6, 7, and 8 to demonstrate the computational efficiency and precision of the 3N2L-FDM. To provide a sufficiently precise reference, the ideal SLD under $m = 200$ is still achieved using the 2L1L-FDM, where the computational cost is 4182.9 s. From the sub-figures (a) in Figs. 6, 7, and 8, the red curves from the 3N2L-FDM are nearer the black ideal SLD than the curves from the SDM, 1L1L-FDM, and 2L1L-FDM. Similarly, in the sub-figures (b) of Figs. 6, 7, and 8, when m is 20 or 40, the SLD from 3N2L-FDM is more accurate than the others. And when m is 80, the curves from the 3H2L-FDM, 2L2L-FDM, and 3N2L-FDM are closer to the ideal SLD when compared with the curve from the 3N1L-FDM.

On the other hand, the computational costs when predicting the SLDs are listed in Table 3, which are the average values after running the corresponding programs three times. It can be seen that the time from the SDM is the longest under the same m, when compared with the other methods. The time cost for the 1L1L-FDM is the lowest because of the low order of the interpolation polynomial used. As the order of the polynomial used to approximate the system state or delayed term increases, the computation cost clearly increases. At the same time, the computational costs for the 3H2L-FDM and 3N2L-FDM are close, whereas the computational precision for the 3N2L-FDM is superior. After the above comparison analysis, it can be concluded that the proposed 3N2L-FDM exhibits better accuracy with a minor loss of computational efficiency.

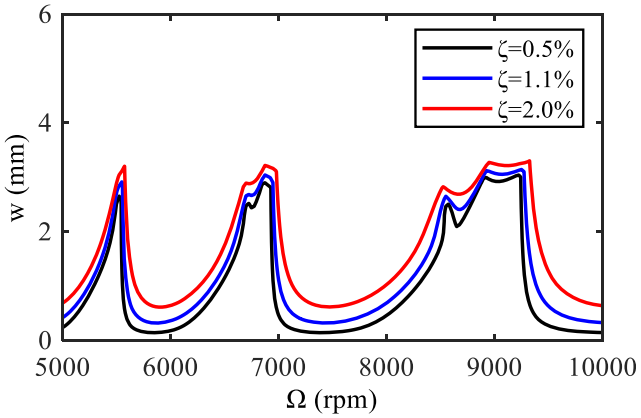

Fig. 10 The SLDs with respect to the varying damping ratio

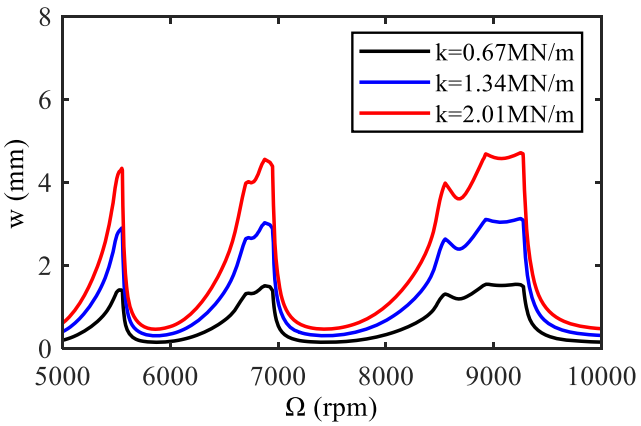

Fig. 9 The SLDs with respect to the varying stiffness

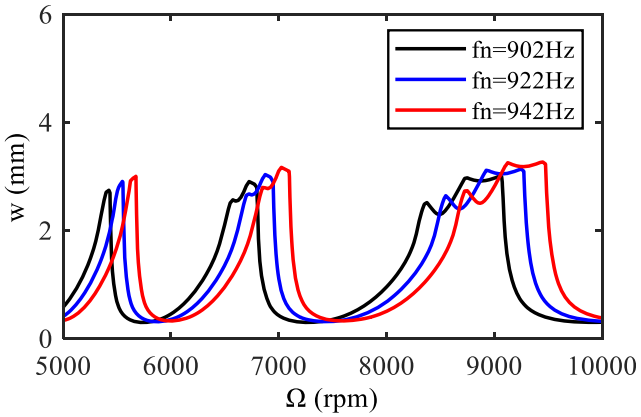

Fig. 11 The SLDs with respect to the varying natural frequency

4 Influence of the dynamic parameters on machining stability

From Eqs. (1) and (23), the dynamic parameters of the machining system may have an important influence on chatter stability, including stiffness k, damping ratio ζ, and modal mass m_t. In this section, the influence of these dynamic parameters on machining stability is investigated and discussed in detail based on the proposed 3N2L-FDM.

4.1 Influence of the stiffness on the SLD

According to dynamics theory, stiffness can be expressed by

$$k = m_t \omega_n^2 \tag{24}$$

where ω_n is the natural frequency with the unit of rad/s. The natural frequency can be expressed in units of Hz, that is, $f_n = \omega_n/2\pi$.

In order to analyze the influence of stiffness on the SLD, the modal masses m_t of 0.02 kg, 0.04 kg, and 0.06 kg are chosen, and thereby the corresponding stiffness k is obtained as 0.67 MN/m, 1.34 MN/m, and 2.01 MN/m, respectively. Other parameters are $\omega_n = 5793.1$ rad/s, $\zeta = 1.1\%$, and $a/D = 1$. The SLDs are calculated by the proposed 3N2L-FDM, and are shown in Fig. 9. It can be clearly observed that the overall lobes shift upward significantly when the stiffness k increases. The increase of the peak value is greater than that of the valley value. This analysis result means that increasing the stiffness of the machining system is beneficial to enlarging the stability zone, which is verified by the developed damping cutters [31, 32].

4.2 Influence of the damping ratio on the SLD

In order to analyze the influence of the damping ratio ζ on the machining stability, the damping ratio ζ was chosen as 0.5%, 1.1%, and 2.0%, respectively, and other parameters are $m_t = 0.04$ kg, $\omega_n = 5793.1$ rad/s, and $a/D = 1$. Then, based on the 3N2L-FDM, the SLDs can be obtained and are shown in Fig. 10. From the figure, when ζ increases, the lobes shift upward, which is similar to our observations in Fig. 9. However, the valley value clearly increases when comparing with the peak value. Similarly, through increasing the damping ratio, the chatter stability can be improved, when the corresponding cutter or toolholder is designed [33, 34].

4.3 Influence of the natural frequency on the SLD

When investigating the influence of the natural frequency on the milling stability, the natural frequencies of 902 Hz, 922 Hz, and 942 Hz are selected, and the other parameters are $m_t = 0.04$ kg, $\zeta = 1.1\%$, and $a/D = 1$. The predicted SLDs are shown in Fig. 11. When f_n changes from 902 to 942 Hz, the lobes shift to the right. This suggests that shifting the lobes, such as adding the additional mass to shift the SLD in ref. [35], is an effective way to achieve specific machining parameters. In addition, it should be noted that the limit cutting depth increases slightly when f_n increases, which can be observed in Fig. 11. However, this seems to disagree with the conclusion that changing f_n has no effect on the limit cutting depth [31]. This is because the stiffness can be increased when f_n increases according to Eq. (24), which can increase the limit cutting depth. Thus, when considering the effect of the change of f_n on the stiffness, changing f_n can not only shift the lobes, but also slightly increase the limit cutting depth.

5 Conclusions

In this work, an improved full-discretization method that combines interpolation of the Newton and Lagrange polynomials is proposed to predict machining stability. The system state and time periodic terms are estimated by the means of the third-order Newton and first-order Lagrange polynomials, respectively. The second-order Lagrange polynomial is used to approximate the delayed term, where its order is determined by comparing the computational performance from the different order conditions. In order to further verify the effectiveness of the proposed 3N2L-FDM, the convergence rates and the SLDs from the different discretization methods are compared, which demonstrates that the 3N2L-FDM provides the best precision with minor loss of computational efficiency. In addition, the influences of the dynamic parameters on the machining stability are analyzed. It can be observed that increasing the stiffness and damping ratio can improve chatter stability, and changing the natural frequency mainly makes the SLD shift horizontally, which can guide improved stability design for the machining system.

Funding This research was funded by the National Natural Science Foundation of China (Grant No. 51975336), the Key Science and Technology Innovation Project of Shandong Province (Grant No. 2019JZZY010112), Key Basic Research Project of Natural Science Foundation in Shandong Province (Grant No. ZR2018ZB0106), and China Scholarship Council (Grant No. 201906220122).

Compliance with ethical standards

Conflict of interest The authors declare that they have no conflict of interest

Appendix 1. The symbols in case I

The symbols in Eq. (10) are given as follows

$$\begin{aligned}
&\mathbf{F}_0 = \boldsymbol{\Phi}_0\\
&\mathbf{F}_{k1} = \left(\boldsymbol{\Phi}_1 - \frac{11\boldsymbol{\Phi}_2}{6\tau} + \frac{\boldsymbol{\Phi}_3}{\tau^2} - \frac{\boldsymbol{\Phi}_4}{6\tau^3}\right)\mathbf{A}_0^{(k)} + \left(\boldsymbol{\Phi}_2 - \frac{11\boldsymbol{\Phi}_3}{6\tau} + \frac{\boldsymbol{\Phi}_4}{\tau^2} - \frac{\boldsymbol{\Phi}_5}{6\tau^3}\right)\mathbf{A}_1^{(k)}\\
&\mathbf{F}_k = \left(\frac{3\boldsymbol{\Phi}_2}{\tau} - \frac{5\boldsymbol{\Phi}_3}{2\tau^2} + \frac{\boldsymbol{\Phi}_4}{2\tau^3}\right)\mathbf{A}_0^{(k)} + \left(\frac{3\boldsymbol{\Phi}_3}{\tau} - \frac{5\boldsymbol{\Phi}_4}{2\tau^2} + \frac{\boldsymbol{\Phi}_5}{2\tau^3}\right)\mathbf{A}_1^{(k)}\\
&\mathbf{F}_{kp1} = \left(-\frac{3\boldsymbol{\Phi}_2}{2\tau} + \frac{2\boldsymbol{\Phi}_3}{\tau^2} - \frac{\boldsymbol{\Phi}_4}{2\tau^3}\right)\mathbf{A}_0^{(k)} + \left(-\frac{3\boldsymbol{\Phi}_3}{2\tau} + \frac{2\boldsymbol{\Phi}_4}{\tau^2} - \frac{\boldsymbol{\Phi}_5}{2\tau^3}\right)\mathbf{A}_1^{(k)}\\
&\mathbf{F}_{kp2} = \left(\frac{\boldsymbol{\Phi}_2}{3\tau} - \frac{\boldsymbol{\Phi}_3}{2\tau^2} + \frac{\boldsymbol{\Phi}_4}{6\tau^3}\right)\mathbf{A}_0^{(k)} + \left(\frac{\boldsymbol{\Phi}_3}{3\tau} - \frac{\boldsymbol{\Phi}_4}{2\tau^2} + \frac{\boldsymbol{\Phi}_5}{6\tau^3}\right)\mathbf{A}_1^{(k)}\\
&\mathbf{F}_{k1m} = \left(\boldsymbol{\Phi}_1 - \frac{\boldsymbol{\Phi}_2}{\tau}\right)\mathbf{B}_0^{(k)} + \left(\boldsymbol{\Phi}_2 - \frac{\boldsymbol{\Phi}_3}{\tau}\right)\mathbf{B}_1^{(k)}\\
&\mathbf{F}_{k1m} = \left(\boldsymbol{\Phi}_1 - \frac{\boldsymbol{\Phi}_2}{\tau}\right)\mathbf{B}_0^{(k)} + \left(\boldsymbol{\Phi}_2 - \frac{\boldsymbol{\Phi}_3}{\tau}\right)\mathbf{B}_1^{(k)}\\
&\mathbf{F}_{km} = \frac{\boldsymbol{\Phi}_2}{\tau}\mathbf{B}_0^{(k)} + \frac{\boldsymbol{\Phi}_3}{\tau}\mathbf{B}_1^{(k)}
\end{aligned} \tag{25}$$

where

$$\begin{aligned}
&\boldsymbol{\Phi}_0 = e^{\mathbf{A}_0\tau}\\
&\boldsymbol{\Phi}_1 = \int_0^\tau e^{\mathbf{A}_0\xi}d\xi = \mathbf{A}_0^{-1}(\boldsymbol{\Phi}_0 - \mathbf{I})\\
&\boldsymbol{\Phi}_2 = \int_0^\tau \xi e^{\mathbf{A}_0\xi}d\xi = \mathbf{A}_0^{-1}(\tau\boldsymbol{\Phi}_0 - \boldsymbol{\Phi}_1)\\
&\boldsymbol{\Phi}_3 = \int_0^\tau \xi^2 e^{\mathbf{A}_0\xi}d\xi = \mathbf{A}_0^{-1}(\tau^2\boldsymbol{\Phi}_0 - 2\boldsymbol{\Phi}_2)\\
&\boldsymbol{\Phi}_4 = \int_0^\tau \xi^3 e^{\mathbf{A}_0\xi}d\xi = \mathbf{A}_0^{-1}(\tau^3\boldsymbol{\Phi}_0 - 3\boldsymbol{\Phi}_3)\\
&\boldsymbol{\Phi}_5 = \int_0^\tau \xi^4 e^{\mathbf{A}_0\xi}d\xi = \mathbf{A}_0^{-1}(\tau^4\boldsymbol{\Phi}_0 - 4\boldsymbol{\Phi}_4)
\end{aligned} \tag{26}$$

The matrix $\boldsymbol{D}_\mathrm{k}$ in Eq. (11) is given as follows:

$$\mathbf{D}_k = \begin{bmatrix}
\mathbf{H}_{11} & \mathbf{H}_{p1} & \mathbf{H}_{p2} & \cdots & \mathbf{0} & \mathbf{H}_{1m} & \mathbf{H}_m\\
\mathbf{I} & \mathbf{0} & \mathbf{0} & \cdots & \mathbf{0} & \mathbf{0} & \mathbf{0}\\
\mathbf{0} & \mathbf{I} & \mathbf{0} & \cdots & \mathbf{0} & \mathbf{0} & \mathbf{0}\\
\mathbf{0} & \mathbf{0} & \mathbf{I} & \cdots & \mathbf{0} & \mathbf{0} & \mathbf{0}\\
\vdots & \vdots & \vdots & \ddots & \vdots & \vdots & \vdots\\
\mathbf{0} & \mathbf{0} & \mathbf{0} & \cdots & \mathbf{I} & \mathbf{0} & \mathbf{0}\\
\mathbf{0} & \mathbf{0} & \mathbf{0} & \cdots & \mathbf{0} & \mathbf{I} & \mathbf{0}
\end{bmatrix} \tag{27}$$

where

$$\begin{aligned}
&\mathbf{H}_{11} = (\mathbf{I} - \mathbf{F}_{k1})^{-1}(\mathbf{F}_0 + \mathbf{F}_k)\\
&\mathbf{H}_{p1} = (\mathbf{I} - \mathbf{F}_{k1})^{-1}\mathbf{F}_{kp1}\\
&\mathbf{H}_{p2} = (\mathbf{I} - \mathbf{F}_{k1})^{-1}\mathbf{F}_{kp2}\\
&\mathbf{H}_{1m} = (\mathbf{I} - \mathbf{F}_{k1})^{-1}\mathbf{F}_{k1m}\\
&\mathbf{H}_m = (\mathbf{I} - \mathbf{F}_{k1})^{-1}\mathbf{F}_{km}
\end{aligned} \tag{28}$$

Appendix 2. The symbols in case II

The symbols in Eq. (16) are listed as follows, in which the symbols $\boldsymbol{F}_{\mathrm{k1}}$, $\boldsymbol{F}_\mathrm{k}$, $\boldsymbol{F}_{\mathrm{kp1}}$, and $\boldsymbol{F}_{\mathrm{kp2}}$ are the same as those in case I.

$$\begin{aligned}
&\mathbf{F}_{k2m} = \left(\frac{\boldsymbol{\Phi}_3}{2\tau^2} - \frac{\boldsymbol{\Phi}_2}{2\tau}\right)\mathbf{B}_0^{(k)} + \left(\frac{\boldsymbol{\Phi}_4}{2\tau^2} - \frac{\boldsymbol{\Phi}_3}{2\tau}\right)\mathbf{B}_1^{(k)}\\
&\mathbf{F}_{k1m} = \left(\boldsymbol{\Phi}_1 - \frac{\boldsymbol{\Phi}_3}{\tau^2}\right)\mathbf{B}_0^{(k)} + \left(\boldsymbol{\Phi}_2 - \frac{\boldsymbol{\Phi}_4}{\tau^2}\right)\mathbf{B}_1^{(k)}\\
&\mathbf{F}_{km} = \left(\frac{\boldsymbol{\Phi}_3}{2\tau^2} + \frac{\boldsymbol{\Phi}_2}{2\tau}\right)\mathbf{B}_0^{(k)} + \left(\frac{\boldsymbol{\Phi}_4}{2\tau^2} + \frac{\boldsymbol{\Phi}_3}{2\tau}\right)\mathbf{B}_1^{(k)}
\end{aligned} \tag{29}$$

where the $\boldsymbol{\Phi}_\mathrm{i}$ ($i = 1$, 2, 3, and 4) are shown in Eq. (26).

The matrix $\boldsymbol{D}_\mathrm{k}$ in case II is given as follows:

$$\mathbf{D}_k = \begin{bmatrix}
\mathbf{H}_{11} & \mathbf{H}_{p1} & \mathbf{H}_{p2} & \cdots & \mathbf{0} & \mathbf{H}_{2m} & \mathbf{H}_{1m} & \mathbf{H}_m\\
\mathbf{I} & \mathbf{0} & \mathbf{0} & \cdots & \mathbf{0} & \mathbf{0} & \mathbf{0} & \mathbf{0}\\
\mathbf{0} & \mathbf{I} & \mathbf{0} & \cdots & \mathbf{0} & \mathbf{0} & \mathbf{0} & \mathbf{0}\\
\mathbf{0} & \mathbf{0} & \mathbf{I} & \cdots & \mathbf{0} & \mathbf{0} & \mathbf{0} & \mathbf{0}\\
\vdots & \vdots & \vdots & \ddots & \vdots & \vdots & \vdots & \vdots\\
\mathbf{0} & \mathbf{0} & \mathbf{0} & \cdots & \mathbf{I} & \mathbf{0} & \mathbf{0} & \mathbf{0}\\
\mathbf{0} & \mathbf{0} & \mathbf{0} & \cdots & \mathbf{0} & \mathbf{I} & \mathbf{0} & \mathbf{0}\\
\mathbf{0} & \mathbf{0} & \mathbf{0} & \cdots & \mathbf{0} & \mathbf{0} & \mathbf{I} & \mathbf{0}
\end{bmatrix} \tag{30}$$

where $\mathbf{H}_{11}$, $\mathbf{H}_{\mathrm{p1}}$, and $\mathbf{H}_{\mathrm{p2}}$ are the same as those in Eq. (27), and $\mathbf{H}_{\mathrm{2m}}$, $\mathbf{H}_{\mathrm{1m}}$, and $\mathbf{H}_\mathrm{m}$ are shown as follows:

$$\begin{aligned}
&\mathbf{H}_{2m} = (\mathbf{I} - \mathbf{F}_{k1})^{-1}\mathbf{F}_{k2m}\\
&\mathbf{H}_{1m} = (\mathbf{I} - \mathbf{F}_{k1})^{-1}\mathbf{F}_{k1m}\\
&\mathbf{H}_m = (\mathbf{I} - \mathbf{F}_{k1})^{-1}\mathbf{F}_{km}
\end{aligned} \tag{31}$$

Appendix 3. The symbols in case III

The symbols in Eq. (19) are listed as follows, where the symbols $\boldsymbol{F}_{\mathrm{k1}}$, $\boldsymbol{F}_\mathrm{k}$, $\boldsymbol{F}_{\mathrm{kp1}}$, and $\boldsymbol{F}_{\mathrm{kp2}}$ are the same as those in case I.

$$\begin{aligned}
&\mathbf{F}_{k3m} = \left(-\frac{\boldsymbol{\Phi}_4}{6\tau^3} + \frac{\boldsymbol{\Phi}_2}{6\tau}\right)\mathbf{B}_0^{(k)} + \left(-\frac{\boldsymbol{\Phi}_5}{6\tau^3} + \frac{\boldsymbol{\Phi}_3}{6\tau}\right)\mathbf{B}_1^{(k)}\\
&\mathbf{F}_{k2m} = \left(\frac{\boldsymbol{\Phi}_4}{2\tau^3} + \frac{\boldsymbol{\Phi}_3}{2\tau^2} - \frac{\boldsymbol{\Phi}_2}{\tau}\right)\mathbf{B}_0^{(k)} + \left(\frac{\boldsymbol{\Phi}_5}{2\tau^3} + \frac{\boldsymbol{\Phi}_4}{2\tau^2} - \frac{\boldsymbol{\Phi}_3}{\tau}\right)\mathbf{B}_1^{(k)}\\
&\mathbf{F}_{k1m} = \left(-\frac{\boldsymbol{\Phi}_4}{2\tau^3} - \frac{\boldsymbol{\Phi}_3}{\tau^2} + \frac{\boldsymbol{\Phi}_2}{2\tau} + \boldsymbol{\Phi}_1\right)\mathbf{B}_0^{(k)} + \left(-\frac{\boldsymbol{\Phi}_5}{2\tau^3} - \frac{\boldsymbol{\Phi}_4}{\tau^2} + \frac{\boldsymbol{\Phi}_3}{2\tau} + \boldsymbol{\Phi}_2\right)\mathbf{B}_1^{(k)}\\
&\mathbf{F}_{km} = \left(\frac{\boldsymbol{\Phi}_4}{6\tau^3} + \frac{\boldsymbol{\Phi}_3}{2\tau^2} + \frac{\boldsymbol{\Phi}_2}{3\tau}\right)\mathbf{B}_0^{(k)} + \left(\frac{\boldsymbol{\Phi}_5}{6\tau^3} + \frac{\boldsymbol{\Phi}_4}{2\tau^2} + \frac{\boldsymbol{\Phi}_3}{3\tau}\right)\mathbf{B}_1^{(k)}
\end{aligned} \tag{32}$$

where the $\boldsymbol{\Phi}_\mathrm{i}$ ($i = 1$, 2, 3, 4, and 5) are shown in Eq. (26).

The matrix $\boldsymbol{D}_\mathrm{k}$ in case III is given as follows:

$$\mathbf{D}_k = \begin{bmatrix}
\mathbf{H}_{11} & \mathbf{H}_{p1} & \mathbf{H}_{p2} & \cdots & \mathbf{0} & \mathbf{H}_{3m} & \mathbf{H}_{2m} & \mathbf{H}_{1m} & \mathbf{H}_m\\
\mathbf{I} & \mathbf{0} & \mathbf{0} & \cdots & \mathbf{0} & \mathbf{0} & \mathbf{0} & \mathbf{0} & 0\\
\mathbf{0} & \mathbf{I} & \mathbf{0} & \cdots & \mathbf{0} & \mathbf{0} & \mathbf{0} & \mathbf{0} & 0\\
\mathbf{0} & \mathbf{0} & \mathbf{I} & \cdots & \mathbf{0} & \mathbf{0} & \mathbf{0} & \mathbf{0} & 0\\
\vdots & \vdots & \vdots & \ddots & \vdots & \vdots & \vdots & \vdots & \vdots\\
\mathbf{0} & \mathbf{0} & \mathbf{0} & \cdots & \mathbf{I} & \mathbf{0} & \mathbf{0} & \mathbf{0} & 0\\
\mathbf{0} & \mathbf{0} & \mathbf{0} & \cdots & \mathbf{0} & \mathbf{I} & \mathbf{0} & \mathbf{0} & \mathbf{0}\\
\mathbf{0} & \mathbf{0} & \mathbf{0} & \cdots & \mathbf{0} & \mathbf{0} & \mathbf{I} & \mathbf{0} & \mathbf{0}\\
\mathbf{0} & \mathbf{0} & \mathbf{0} & \cdots & \mathbf{0} & \mathbf{0} & \mathbf{0} & \mathbf{I} & \mathbf{0}
\end{bmatrix} \tag{33}$$

where $\mathbf{H}_{11}$, $\mathbf{H}_{p1}$, and $\mathbf{H}_{p2}$ are the same as those in Eq. (27), and $\mathbf{H}_{3m}$, $\mathbf{H}_{2m}$, $\mathbf{H}_{1m}$, and $\mathbf{H}_{m}$ are shown as follows:

$$\begin{aligned}\mathbf{H}_{3m} &= (\mathbf{I}-\mathbf{F}_{k1})^{-1}\mathbf{F}_{k3m}\\ \mathbf{H}_{2m} &= (\mathbf{I}-\mathbf{F}_{k1})^{-1}\mathbf{F}_{k2m}\\ \mathbf{H}_{1m} &= (\mathbf{I}-\mathbf{F}_{k1})^{-1}\mathbf{F}_{k1m}\\ \mathbf{H}_{m} &= (\mathbf{I}-\mathbf{F}_{k1})^{-1}\mathbf{F}_{km}\end{aligned} \tag{34}$$

Appendix 4. The symbols in case IV

The symbols in Eq. (22) are listed as follows, where the symbols $\boldsymbol{F}_{k1}$, $\boldsymbol{F}_{k}$, $\boldsymbol{F}_{kp1}$, and $\boldsymbol{F}_{kp2}$ are the same as those in case I.

$$\begin{aligned}\mathbf{F}_{k4m} &= \left(\frac{\boldsymbol{\Phi}_5}{24\tau^4}+\frac{\boldsymbol{\Phi}_4}{12\tau^3}-\frac{\boldsymbol{\Phi}_3}{24\tau^2}-\frac{\boldsymbol{\Phi}_2}{12\tau}\right)\mathbf{B}_0^{(k)}+\left(\frac{\boldsymbol{\Phi}_6}{24\tau^3}+\frac{\boldsymbol{\Phi}_5}{12\tau^3}-\frac{\boldsymbol{\Phi}_4}{24\tau^2}-\frac{\boldsymbol{\Phi}_3}{12\tau}\right)\mathbf{B}_1^{(k)}\\ \mathbf{F}_{k3m} &= \left(-\frac{\boldsymbol{\Phi}_5}{6\tau^4}-\frac{\boldsymbol{\Phi}_4}{2\tau^3}+\frac{\boldsymbol{\Phi}_3}{6\tau^2}+\frac{\boldsymbol{\Phi}_2}{2\tau}\right)\mathbf{B}_0^{(k)}+\left(-\frac{\boldsymbol{\Phi}_6}{6\tau^4}-\frac{\boldsymbol{\Phi}_5}{2\tau^3}+\frac{\boldsymbol{\Phi}_4}{6\tau^2}+\frac{\boldsymbol{\Phi}_3}{2\tau}\right)\mathbf{B}_1^{(k)}\\ \mathbf{F}_{k2m} &= \left(\frac{\boldsymbol{\Phi}_5}{4\tau^4}+\frac{\boldsymbol{\Phi}_4}{\tau^3}+\frac{\boldsymbol{\Phi}_3}{4\tau^2}-\frac{3\boldsymbol{\Phi}_2}{2\tau}\right)\mathbf{B}_0^{(k)}+\left(\frac{\boldsymbol{\Phi}_6}{4\tau^4}+\frac{\boldsymbol{\Phi}_5}{\tau^3}+\frac{\boldsymbol{\Phi}_4}{4\tau^2}-\frac{\mathbf{3}\boldsymbol{\Phi}_3}{2\tau}\right)\mathbf{B}_1^{(k)}\\ \mathbf{F}_{k1m} &= \left(-\frac{\boldsymbol{\Phi}_5}{6\tau^4}-\frac{5\boldsymbol{\Phi}_4}{6\tau^3}-\frac{\mathbf{5}\boldsymbol{\Phi}_3}{6\tau^2}+\frac{5\boldsymbol{\Phi}_2}{6\tau}+\boldsymbol{\Phi}_1\right)\mathbf{B}_0^{(k)}+\left(-\frac{\boldsymbol{\Phi}_6}{6\tau^4}-\frac{\mathbf{5}\boldsymbol{\Phi}_5}{6\tau^3}-\frac{\mathbf{5}\boldsymbol{\Phi}_4}{6\tau^2}+\frac{\mathbf{5}\boldsymbol{\Phi}_3}{6\tau}+\boldsymbol{\Phi}_2\right)\mathbf{B}_1^{(k)}\\ \mathbf{F}_{km} &= \left(-\frac{\boldsymbol{\Phi}_5}{24\tau^4}+\frac{\boldsymbol{\Phi}_4}{4\tau^3}+\frac{11\boldsymbol{\Phi}_3}{24\tau^2}+\frac{\boldsymbol{\Phi}_2}{4\tau}\right)\mathbf{B}_0^{(k)}+\left(\frac{\boldsymbol{\Phi}_6}{24\tau^4}+\frac{\boldsymbol{\Phi}_5}{4\tau^3}+\frac{11\boldsymbol{\Phi}_4}{24\tau^2}+\frac{\boldsymbol{\Phi}_3}{4\tau}\right)\mathbf{B}_1^{(k)}\end{aligned} \tag{35}$$

where the $\boldsymbol{\Phi}_i$ ($i = 1, 2, 3, 4$, and 5) are shown in Eq. (26), and $\boldsymbol{\Phi}_6$ is expressed by

$$\boldsymbol{\Phi}_6 = \int_0^\tau \xi^5 e^{\mathbf{A}_0\xi}d\xi = \mathbf{A}_0^{-1}\left(\tau^5\boldsymbol{\Phi}_0-5\boldsymbol{\Phi}_5\right) \tag{36}$$

The matrix $\boldsymbol{D}_k$ in case IV is given as follows:

$$\mathbf{D}_k = \begin{bmatrix} \mathbf{H}_{11} & \mathbf{H}_{p1} & \mathbf{H}_{p2} & \cdots & \mathbf{0} & \mathbf{H}_{4m} & \mathbf{H}_{3m} & \mathbf{H}_{2m} & \mathbf{H}_{1m} & \mathbf{H}_{m} \\ \mathbf{I} & \mathbf{0} & \mathbf{0} & \cdots & \mathbf{0} & \mathbf{0} & \mathbf{0} & \mathbf{0} & \mathbf{0} & 0 \\ \mathbf{0} & \mathbf{I} & \mathbf{0} & \cdots & \mathbf{0} & \mathbf{0} & \mathbf{0} & \mathbf{0} & \mathbf{0} & 0 \\ \mathbf{0} & \mathbf{0} & \mathbf{I} & \cdots & \mathbf{0} & \mathbf{0} & \mathbf{0} & \mathbf{0} & \mathbf{0} & 0 \\ \vdots & \vdots & \vdots & \ddots & \vdots & \vdots & \vdots & \vdots & \vdots & \vdots \\ \mathbf{0} & \mathbf{0} & \mathbf{0} & \cdots & \mathbf{I} & \mathbf{0} & \mathbf{0} & \mathbf{0} & \mathbf{0} & 0 \\ \mathbf{0} & \mathbf{0} & \mathbf{0} & \cdots & \mathbf{0} & \mathbf{I} & \mathbf{0} & \mathbf{0} & \mathbf{0} & \mathbf{0} \\ \mathbf{0} & \mathbf{0} & \mathbf{0} & \cdots & \mathbf{0} & \mathbf{0} & \mathbf{I} & \mathbf{0} & \mathbf{0} & \mathbf{0} \\ \mathbf{0} & \mathbf{0} & \mathbf{0} & \cdots & \mathbf{0} & \mathbf{0} & \mathbf{0} & \mathbf{I} & \mathbf{0} & \mathbf{0} \\ \mathbf{0} & \mathbf{0} & \mathbf{0} & \cdots & \mathbf{0} & \mathbf{0} & \mathbf{0} & \mathbf{0} & \mathbf{I} & \mathbf{0} \end{bmatrix} \tag{37}$$

where $\mathbf{H}_{11}$, $\mathbf{H}_{p1}$, and $\mathbf{H}_{p2}$ are the same as those in Eq. (27), and $\mathbf{H}_{4m}$, $\mathbf{H}_{3m}$, $\mathbf{H}_{2m}$, $\mathbf{H}_{1m}$, and $\mathbf{H}_{m}$ are shown as follows:

$$\begin{aligned}\mathbf{H}_{4m} &= (\mathbf{I}-\mathbf{F}_{k1})^{-1}\mathbf{F}_{k4m}\\ \mathbf{H}_{3m} &= (\mathbf{I}-\mathbf{F}_{k1})^{-1}\mathbf{F}_{k3m}\\ \mathbf{H}_{2m} &= (\mathbf{I}-\mathbf{F}_{k1})^{-1}\mathbf{F}_{k2m}\\ \mathbf{H}_{1m} &= (\mathbf{I}-\mathbf{F}_{k1})^{-1}\mathbf{F}_{k1m}\\ \mathbf{H}_{m} &= (\mathbf{I}-\mathbf{F}_{k1})^{-1}\mathbf{F}_{km}\end{aligned} \tag{38}$$

References

1. Quintana G, Ciurana J (2011) Chatter in machining processes: a review. Int J Mach Tools Manuf 51(5):363–376
2. Munoa J, Beudaert X, Dombovari Z, Altintas Y, Budak E, Brecher C, Stepan G (2016) Chatter suppression techniques in metal cutting. CIRP Ann-Manuf Technol 65(2):785–808
3. Zhang XJ, Xiong CH, Ding Y, Feng MJ, Xiong YL (2012) Milling stability analysis with simultaneously considering the structural mode coupling effect and regenerative effect. Int J Mach Tools Manuf 53(1):127–140
4. Ji YJ, Wang XB, Liu ZB, Wang HJ, Jiao L, Zhang L, Huang T (2018) Milling stability prediction with simultaneously considering the multiple factors coupling effects-regenerative effect, mode coupling, and process damping. Int J Adv Manuf Technol 97(5):2509–2527

5. Altintaş Y, Budak E (1995) Analytical prediction of stability lobes in milling. CIRP Ann-Manuf Technol 44(1):357–362
6. Altintas Y, Stepan G, Merdol D, Dombovari Z (2008) Chatter stability of milling in frequency and discrete time domain. CIRP J Manuf Sci Technol 1(1):35–44
7. Bayly PV, Halley JE, Mann BP, Davies MA (2003) Stability of interrupted cutting by temporal finite element analysis. J Manuf Sci Eng 125(2):220–225
8. Ding Y, Zhu LM, Zhang XJ, Ding H (2011) Numerical integration method for prediction of milling stability. J Manuf Sci Eng 133(3): 1–9
9. Liang XG, Yao ZQ, Luo L, Hu J (2013) An improved numerical integration method for predicting milling stability with varying delayed. Int J Adv Manuf Technol 68(9):1967–1976
10. Zhang Z, Li HG, Meng G, Liu C (2015) A novel approach for the prediction of the milling stability based on the Simpson method. Int J Mach Tools Manuf 99:43–47
11. Ozoegwu CG (2016) High order vector numerical integration schemes applied in state space milling stability analysis. Appl Math Comput 273:1025–1040
12. Insperger T, Stépán G (2004) Updated semi-discretization method for periodic delay-differential equations with discrete delay. Int J Numer Methods Eng 61:117–141
13. Insperger T (2010) Full-discretization and semi-discretization for milling stability prediction: some comments. Int J Mach Tools Manuf 50(7):658–662
14. Ding Y, Zhu LM, Zhang XJ, Ding H (2010) A full-discretization method for prediction of milling stability. Int J Mach Tools Manuf 50(5):502–509
15. Ding Y, Zhu LM, Zhang XJ, Ding H (2010) Second-order full-discretization method for milling stability prediction. Int J Mach Tools Manuf 50(10):926–932
16. Zhang J, Liu CY (2019) Chatter stability prediction of ball-end milling considering multi-mode regenerations. Int J Adv Manuf Technol 100(1):131–142
17. Tang XW, Peng FY, Yan R, Gong YH, Li YT, Jiang LL (2017) Accurate and efficient prediction of milling stability with updated full-discretization method. Int J Adv Manuf Technol 88(9):2357–2368
18. Qin CJ, Tao JF, Liu CL (2019) A novel stability prediction method for milling operations using the holistic-interpolation scheme. Proc IMechE Term C: J Mech Eng Sci 233(13):4463–4475
19. Guo Q, Sun YW, Jiang Y (2012) On the accurate calculation of milling stability limits using third-order full-discretization method. Int J Mach Tools Manuf 62:61–66
20. Liu YL, Zhang DH, Wu BH (2012) An efficient full-discretization method for prediction of milling stability. Int J Mach Tools Manuf 63:44–48
21. Ji YJ, Wang XB, Liu ZB, Wang HJ, Yan ZH (2018) An updated full-discretization milling stability prediction method based on the higher-order Hermite-Newton interpolation polynomial. Int J Adv Manuf Technol 95(5):2227–2242
22. Yang WA, Huang C, Cai XL, You YP (2020) Effective and fast prediction of milling stability using a precise integration-based third-order full-discretization method. Int J Adv Manuf Technol 106(9):4477–4498
23. Ozoegwu CG (2014) Least squares approximated stability boundaries of milling process. Int J Mach Tools Manuf 79:24–30
24. Ozoegwu CG, Omenyi SN, Ofochebe SM (2015) Hyper-third order full-discretization methods in milling stability prediction. Int J Mach Tools Manuf 92:1–9
25. Zhou K, Feng PF, Xu C, Zhang JF, Wu ZJ (2017) High-order full-discretization methods for milling stability prediction by interpolating the delay term of time-delayed differential equations. Int J Adv Manuf Technol 93(5):2201–2214
26. Dai YB, Li HK, Hao BT (2018) An improved full-discretization method for chatter stability prediction. Int J Adv Manuf Technol 96(9):3503–3510
27. Li MZ, Zhang GJ, Huang Y (2013) Complete discretization scheme for milling stability prediction. Nonlinear Dyn 71(1):187–199
28. Sun T, Qin LF, Fu YC, Hou JM (2019) Chatter stability of orthogonal turn-milling analyzed by complete discretization method. Precis Eng 56:87–95
29. Xie Q (2016) Milling stability prediction using an improved complete discretization method. Int J Adv Manuf Technol 83(5):815–821
30. Li ZQ, Yang ZK, Peng YR, Zhu F, Ming XZ (2016) Prediction of chatter stability for milling process using Runge-Kutta-based complete discretization method. Int J Adv Manuf Technol 86(1):943–952
31. Liu Y, Liu ZQ, Song QH, Wang B (2016) Development of constrained layer damping toolholder to improve chatter stability in end milling. Int J Mech Sci 117:299–308
32. Xia Y, Wan Y, Luo XC, Wang HW, Gong N, Cao JL, Liu ZQ, Song QH (2020) Development of a toolholder with high dynamic stiffness for mitigating chatter and improving machining efficiency in face milling. Mech Syst Signal Process 145:106928
33. Xia Y, Wan Y, Luo XC, Wang HW, Gong N, Cao JL, Song QH, Liu ZQ (2020) Chatter suppression in large overhang face milling using a toolholder with high dynamic performance. Int J Adv Manuf Technol 108:1713–1724
34. Yang YQ, Wang YF, Liu Q (2018) Design of a milling cutter with large length–diameter ratio based on embedded passive damper. J Vib Control 25(3):506–516
35. Wan M, Dang XB, Zhang WH, Yang Y (2018) Optimization and improvement of stable processing condition by attaching additional masses for milling of thin-walled workpiece. Mech Syst Signal Process 103:196–215